



HAL
open science

Accurate intravoxel incoherent motion parameter estimation using Bayesian fitting and reduced number of low b-values

Chen Ye, Daoyun Xu, Yongbin Qin, Lihui Wang, Rongpin Wang, Wuchao Li,
Zixiang Kuai, Yuemin Zhu

► To cite this version:

Chen Ye, Daoyun Xu, Yongbin Qin, Lihui Wang, Rongpin Wang, et al.. Accurate intravoxel incoherent motion parameter estimation using Bayesian fitting and reduced number of low b-values. *Medical Physics*, 2020, 47 (9), pp.4372-4385. 10.1002/mp.14233 . hal-03705457

HAL Id: hal-03705457

<https://hal.science/hal-03705457>

Submitted on 2 May 2024

HAL is a multi-disciplinary open access archive for the deposit and dissemination of scientific research documents, whether they are published or not. The documents may come from teaching and research institutions in France or abroad, or from public or private research centers.

L'archive ouverte pluridisciplinaire **HAL**, est destinée au dépôt et à la diffusion de documents scientifiques de niveau recherche, publiés ou non, émanant des établissements d'enseignement et de recherche français ou étrangers, des laboratoires publics ou privés.

1 **Accurate Intravoxel Incoherent Motion Parameter**
2 **Estimation Using Bayesian Fitting and Reduced**
3 **Number of Low b-Values**

4
5 Chen Ye¹, Daoyun Xu^{1*}, Yongbin Qin¹, Lihui Wang¹, Rongpin Wang²,
6 Wuchao Li², Zixiang Kuai³ and Yuemin Zhu⁴

7 ¹Key Laboratory of Intelligent Medical Image Analysis and Precise
8 Diagnosis of Guizhou Province, School of Computer Science and
9 Technology, Guizhou University, Guiyang, China.

10 ²Department of Radiology, Guizhou Provincial People's Hospital,
11 Guiyang, China

12 ³Harbin Medical University Cancer Hospital, Harbin, China

13 ⁴Univ Lyon, INSA Lyon, CNRS, INSERM, CREATIS UMR 5220,
14 U1206, F-69621, Lyon, France

15 Running title: IVIM parameter mapping of brain tumors

16
17 *Correspondence: Daoyun Xu, Ph.D.

18 Address : College of Computer Science and Technology, University of Guizhou,

19 Huaxi District, Guiyang, China 550025.

20 **Email:** dyxu@gzu.edu.cn

21

22 **Abstract**

23 **Purpose:** Intravoxel incoherent motion (IVIM) magnetic resonance imaging is a potential non-invasive
24 technique for the diagnosis of brain tumors. However, perfusion-related parameter mapping is a
25 persistent problem. The purpose of this paper is to investigate the IVIM parameter mapping of brain
26 tumors using Bayesian fitting and low b-values.

27 **Methods:** Bayesian shrinkage prior (BSP) fitting method and different low b-value distributions were
28 used to estimate IVIM parameters (diffusion D , pseudo-diffusion D^* , perfusion fraction F). The results
29 were compared to those obtained by least-squares (LSQ) on both simulated and in vivo brain data.
30 Relative error (RE) and reproducibility were used to evaluate the results. The differences of IVIM
31 parameters between brain tumor and normal regions were compared and used to assess the
32 performance of Bayesian fitting in the IVIM application of brain tumor.

33 **Results:** In tumor regions, the value of D^* tended to be decreased when the number of low b-values
34 was insufficient, especially with LSQ. BSP required less low b-values than LSQ for the correct
35 estimation of perfusion parameters of brain tumors. The IVIM parameter maps of brain tumors yielded
36 by BSP had smaller variability, lower RE and higher reproducibility with respect to those obtained by
37 LSQ. Obvious differences were observed between tumor and normal regions in parameters D ($p < 0.05$)
38 and F ($p < 0.001$), especially F . BSP generated fewer outliers than LSQ, and distinguished better tumors
39 from normal regions in parameter F .

40 **Conclusions:** IVIM parameters clearly allow brain tumors to be differentiated from normal regions.
41 Bayesian fitting yields robust IVIM parameter mapping with fewer outliers and requires less low
42 b-values than LSQ for the parameter estimation.

43 Keywords: IVIM; Bayesian shrinkage prior; low b-values; least squares; brain tumor; perfusion.

44 **1. Introduction**

45 Intravoxel incoherent motion (IVIM) magnetic resonance imaging technique, initially introduced
46 by Le Bihan et al.¹, aims to separate water molecule diffusion (D) component and microvascular
47 perfusion or pseudo-diffusion (D^*) component in the diffusion-weighted (DW) signals of tissues. By
48 simplicity, in what follows, “perfusion” and “pseudo-diffusion” will be used interchangeably.
49 Perfusion-related information (pseudo-diffusion D^* , perfusion fraction F) was shown to be able to

50 diagnose brain tumors, such as tumor grading²⁻⁵ and differentiation of recurrent tumors from
51 post-treatment effects.^{6,7}

52 However, reliable estimation of perfusion-related parameters is a persistent problem.^{4, 8-12} The
53 most common approach to obtaining IVIM parameter maps is the nonlinear least squares (LSQ)
54 method based on the Levenberg-Marquardt algorithm or similar ones.^{7, 13-17} The LSQ method consists
55 in estimating the parameters by solving a regression problem, namely by minimizing the residual
56 between actual and fitted DW signals. Because of the nonlinear structure of IVIM model, one can only
57 obtain the solution of the objective function in an approximate way. To cope with this problem, many
58 researchers approximated the nonlinear DW signal attenuation by a log-linear model and only diffusion
59 D was taken as the decay rate parameter.^{13, 18} However, such modified model does not take into account
60 the independent characterization of diffusion and perfusion components.¹⁸

61 To improve the robustness of LSQ fitting, an alternative approach, called the segmented least
62 squares fitting,^{7, 13-16} is used. The method assumes that the impact of D^* on DW signals can be
63 neglected at high b-values (> 200 s/mm²). It consists of first fitting the diffusion parameter D (and S_0
64 that is used to estimate F) using a mono-exponential model, then calculating the perfusion fraction F
65 with the fitted S_0 signal, and finally estimating the pseudo-diffusion parameter D^* using nonlinear least
66 squares fitting. However, estimating the parameters using such approach causes bias errors due to the
67 assumption on the influence of D^* at high b-values.

68 All the limitations mentioned above are due to LSQ fitting itself. More recently, Bayesian
69 methods have been proposed to solve the regression problem in a probabilistic manner. Bayesian
70 methods estimate IVIM parameters by maximizing a posterior probability of IVIM parameters given
71 the observed signal.¹⁸⁻²¹ Freiman et al. obtained the improved IVIM parameter mapping using Bayesian
72 spatial homogeneity prior (FBM).¹⁸ Orton et al. tried to reduce the outlying estimation by using
73 Bayesian Gaussian shrinkage prior (BSP).¹⁹ However, solving the regression problem using the
74 Bayesian methods also has some limitations, such as the dependence on tissue heterogeneity. So far,
75 Bayesian methods were mainly applied to organs such as liver^{18, 19} and heart.²⁰

76 Meanwhile, b-value being an imaging parameter that reflects the measurement sensitivity to
77 diffusion related to the strength and duration of diffusion gradients, the estimation of D^* is often
78 affected by the number of low b-values ($b < 50$ s/mm²), especially for organs having high
79 pseudo-diffusion coefficients, such as liver²²⁻²⁵ and kidney.²⁶ It is generally recognized that brain is a

80 low-perfusion tissue. However, previously reported studies showed that hyper perfusion was found in
81 brain tumor regions, in terms of F ^{2, 3, 5, 10, 11, 27, 28} and D^* .⁴ Therefore, further study of the effect of low
82 b-values on the perfusion-related parameters of brain tumors appears interesting and necessary.

83 The present work aims to investigate the IVIM parameter mapping of brain tumors using Bayesian
84 fitting and low b-values. To this end, BSP fitting method and different low b-value distributions were
85 used to estimate IVIM parameters (D , D^* and F). The results were compared to those obtained by LSQ
86 fitting on both simulated and in vivo data.

87 2. Materials and Methods

88 2.1. Simulation

89 In order to evaluate the joint effect of low b-values and Bayesian fitting on IVIM parameter
90 estimation, we used a bi-exponential model with noise¹⁹ to simulate IVIM signals,

$$91 S_n = S_0(Fe^{-b_n D^*} + (1-F)e^{-b_n D}) + \varepsilon_n, \quad (1)$$

92 where S_n is the signal measured at the b-value b_n , S_0 the signal with no diffusion weighting, F the
93 perfusion flow fraction, D^* the pseudo-diffusion coefficient, D the diffusion coefficient, and ε_n the
94 additive noise.

95 In the simulation, to investigate the effect of low b-values, various b-value configurations with
96 different number of low b-values ($0 < b < 50$ s/mm²) were used: with four low b-values (0, 10, 20, 30, 40,
97 50, 70, 100, 200, 400, 600, 800, 1000 s/mm²), with three low b-values (0, 20, 30, 40, 50, 70, 100, 200,
98 400, 600, 800, 1000 s/mm²), with two low b-values (0, 30, 40, 50, 70, 100, 200, 400, 600, 800, 1000
99 s/mm²), with 1 low b-value (0, 40, 50, 70, 100, 200, 400, 600, 800, 1000 s/mm²), and without low
100 b-value (0, 50, 70, 100, 200, 400, 600, 800, 1000 s/mm²). Considering the influence of noise, Gaussian
101 noise was added to signals with four different signal-to-noise ratios (SNRs): 20, 40, 60, and 80. The
102 SNR was calculated as the ratio of mean signal intensity to standard deviation of noise intensity on b0
103 image.^{14, 29} Meanwhile, since noise models may impact the performance of fitting methods, Rician noise
104 model was also considered by adding complex Gaussian noise to each signal and calculating the
105 magnitude. The different SNRs were: 2, 10, 20, and 80. For the simulations, the tumor regions of in vivo
106 brain images were selected and the corresponding IVIM parameters at each voxel of the tumor region

107 were estimated by LSQ method. The so obtained parameters D^* , D and F were then used as the
108 ground-truth for the simulation. Considering that low b-values for different perfusion regions have
109 different effects on parameter estimation, two different sets of data with different mean pseudo-diffusion
110 coefficients (high/low, $45.8/6.9 \times 10^{-3} \text{ mm}^2/\text{s}$) were simulated.

111 Using Eq. (1) and the simulation parameters mentioned above, realistic DW images were
112 simulated and subsequent IVIM parameters were estimated from the simulated DW images with
113 Gaussian noise using LSQ and BSP fitting methods respectively. After that, a quantitative analysis is
114 performed by comparing the estimated IVIM parameters and the ground-truth. Furthermore, the
115 parameter estimation performance of BSP method with different noise models and different number of
116 low b-values was evaluated on simulated DW images with Rician noise.

117 On the other hand, since the performance of LSQ or BSP may be affected by the heterogeneity of
118 IVIM parameters in ROI, LSQ and BSP were investigated on heterogeneous regions. To do this, a ROI of
119 a healthy brain was first selected. Then, if IVIM parameter maps calculated using LSQ on the ROI were
120 heterogeneous, the estimated parameters at each voxel of the ROI were used as the ground-truth for the
121 simulation. Rician noise was considered by adding complex Gaussian noise to each signal and
122 calculating the magnitude,^{13, 30} for different SNRs (20, 40, 60, 80). Finally, BSP and LSQ were
123 performed on the ROI using different number of low b-values.

124 Finally, investigations on homogeneous regions were also performed. The IVIM parameters for the
125 simulation were set according to previous studies on brain⁴: D (high/low)= $2.69/0.71 \times 10^{-3} \text{ mm}^2/\text{s}$, D^*
126 (high/low)= $49/5.81 \times 10^{-3} \text{ mm}^2/\text{s}$, F (high/low)= $0.18/0.1$. The simulated region was an 80×80 matrix
127 containing eight (corresponding to eight combinations because there are three IVIM parameters, each of
128 them has two values high and low) rectangular subregions of equal size. In each subregion (rectangle),
129 the IVIM parameter value was set as a constant (high or low). The parameter value of the intermediate
130 regions outside the eight subregions was set to the average of high and low values. In this way, different
131 homogeneous regions were obtained (Fig. 6). Rician noise was added to signals with different SNRs: 20,
132 40, 60 and 80. After that, BSP and LSQ were performed on these homogenous regions using different
133 number of low b-values.

134 2.2. DW image acquisitions

135 The present work was approved by the local Ethics Committee. Informed consent was obtained
136 from each patient. DWI data of eight (four tumor and four normal) human brains were acquired with
137 3.0 Tesla MRI scanner (GE Discovery MR750). The acquisition protocol is as follows: echo planar
138 imaging (EPI) sequence; 256x256 mm field of view; 128x128 matrix; 5 mm slice thickness;
139 TE/TR=77/2800 ms; b-values are 0, 10, 20, 30, 40, 50, 70, 100, 200,400, 600, 800 and 1000 s/mm²;
140 diffusion gradient was in three orthogonal directions and trace-weighting was applied. Four tumor
141 ROIs and the corresponding four normal ROIs from different subjects were selected for the analysis.
142 To reduce the influence of noise, DW scanning of the same brain was repeated 2 times and the scans
143 were then averaged to improve the SNR^{29,31}. The SNRs of in vivo brains at the highest b-value ranged
144 from 25.41 to 38.78, and the averaged SNR is 34.74. The SNR was calculated as the ratio of the mean
145 signal of b1000 image (the highest b-value) to the standard deviation of noise. The noise was estimated
146 from background region that did not present contaminations by ghosting or flow artifacts.³²

147 In order to study the effect of low b-values, different number of low b-values were used in the
148 fitting process, which are the same as those used in the simulation described above.

149 **2.3. Estimation of IVIM parameters.**

150 **2.3.1. Least Squares Fitting**

151 The LSQ method implemented in the present study is the commonly used one in practical
152 applications. It consists in estimating the IVIM parameters by minimizing the difference between
153 predicted and original signals:

$$154 \min \sum_{n=0}^N (S_n - S'_n)^2, \quad (2)$$

155 where S_n is the original signal, and S'_n the predicted signal fitted by LSQ.

156 In the present work, considering that the brain is a low-perfusion tissue, the segmented LSQ method
157 may lead to bias error; we therefore used the traditional LSQ method to evaluate the parameters in a
158 whole process. The initial values of D and F for LSQ estimation were chosen according to the results
159 given by the segmented LSQ, and D^* was set as the common value ($D^*=20 \times 10^{-3} \text{ mm}^2/\text{s}$) of brain
160 according to previous studies.⁴

161 In order to improve the robustness of fitting, constraints on IVIM parameters were used as in ¹⁹:
 162 $0.0005 \leq F \leq 0.9995$; $0.0045 \leq D \leq 18$ ($\times 10^{-3}$ mm²/s); $0.034 \leq D^* \leq 1000$ ($\times 10^{-3}$ mm²/s).

163 2.3.2. Bayesian Shrinkage Prior Inference

164 The BSP method is based on using Gaussian shrinkage prior. The fitting process aims to
 165 maximize a joint posterior probability and is realized by using a Markov chain Monte Carlo (MCMC)
 166 method. The Bayesian modeling process is described as follows.¹⁹

167 Using the IVIM model of Eq. (1), the data Gaussian likelihood reads:

$$168 \quad p(S | F, D, D^*, S_0, \sigma_s^2) = (2\pi\sigma_s^2)^{-N/2} \exp\left(-\frac{1}{2\sigma_s^2} \sum_{n=1}^N (S_n - S_0 g_n)^2\right), \quad (3)$$

169 where $S = [S_1, S_2, \dots, S_N]^T$, $g_n = F e^{-b_n D^*} + (1-F) e^{-b_n D}$, σ_s^2 is the variance of the error term \mathcal{E}_n in Eq.
 170 (1) with Gaussian distribution, and N is the number of b-values.

171 In this model, the parameters S_0 and σ_s^2 were marginalized out, as described by Orton et al.,
 172 and the marginalized Gaussian likelihood can be written as:

$$173 \quad p(S | F, D, D^*) \propto [S^T S - (S^T g)^2 / (g^T g)]^{-N/2}. \quad (4)$$

174 where $g = [g_1, g_2, \dots, g_n]^T$ is a vector containing the expected signal g_n at the n^{th} b-value.

175 The shrinkage prior is assumed to be a multivariate Gauss distribution and can be represented as:

$$176 \quad p(\theta_i | \mu, \Sigma_\mu) = |2\pi\Sigma_\mu|^{-1/2} \exp\left(-\frac{1}{2}(\theta_i - \mu)^T \Sigma_\mu^{-1} (\theta_i - \mu)\right), \quad (5)$$

177 where $\theta = (f, d, d^*)$ is a vector including the transformed IVIM parameters: $f = \ln(F) - \ln(1-F)$,
 178 $d = \ln D$ and $d^* = \ln D^*$. $\mu = (\mu_f, \mu_d, \mu_{d^*})$ is a vector containing the mean values of the transformed
 179 parameter in ROI, Σ_μ is the corresponding covariance matrix, and i denotes the current pixel.

180 Given the observed data, the posterior probability of IVIM parameters estimated at each pixel can
 181 be expressed as:

$$182 \quad p(\theta_{1:M}, \mu, \Sigma_\mu | S_{1:M}) \propto \prod_{i=1}^M p(S_i | \theta_i) p(\theta_i | \mu, \Sigma_\mu), \quad (6)$$

183 where $\theta_{1:M} = [\theta_1, \theta_2, \dots, \theta_M]$, $S_{1:M} = [S_1, S_2, \dots, S_M]$, and M is the number of pixels.

184 The iterative fitting process was realized by MCMC algorithm as illustrated in Fig. 1.

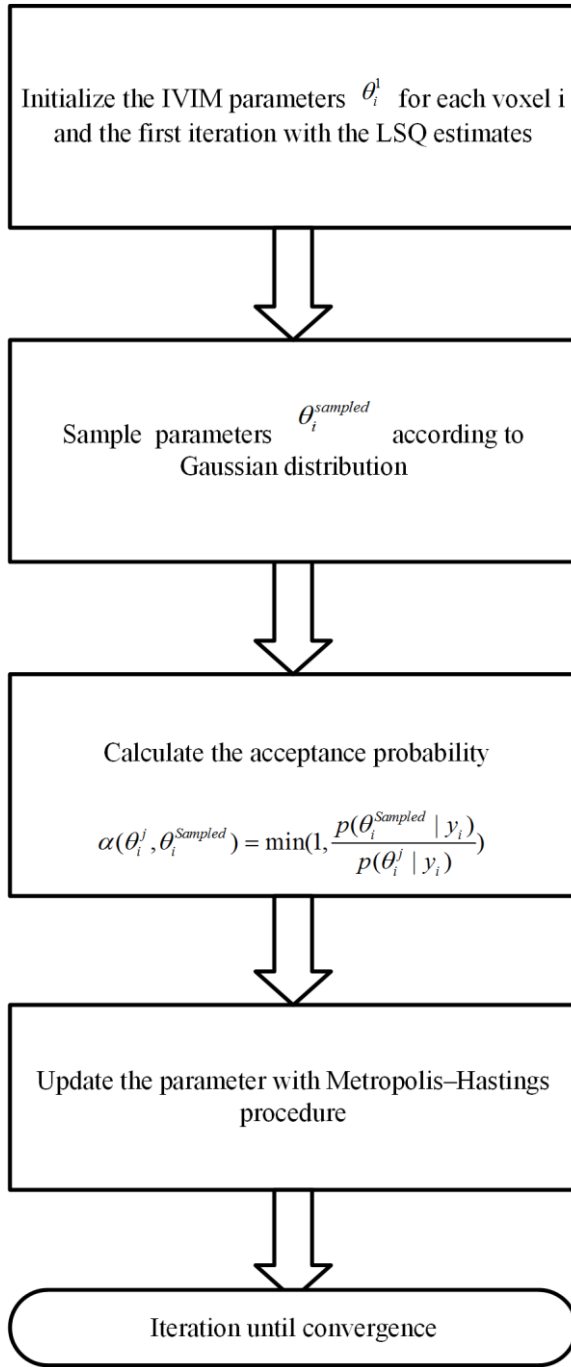


Fig. 1 Flowchart of BSP fitting.

In addition, the additive noise \mathcal{E}_n in Eq. (1) is often assumed to be Gaussian due to the fact that noise in MRI is nearly governed by Gaussian distribution when $\text{SNR} > 2$.³³ Rician distribution noise is however considered when magnitude data is used and SNR is low.^{21,33} The likelihood function based on Rician noise can be expressed as:

$$p(S | F, D, D^*, S_0, \sigma_s^2) = \frac{S_n}{\sigma_s^2} \exp\left(-\frac{1}{2\sigma_s^2}(S_n^2 + S'(b_n)^2)\right) I_0\left(\frac{S_n S'(b_n)}{\sigma_s^2}\right) \quad (7)$$

192 where S_n is the measured signal at b_n , $S'(b_n)$ the expected signal at b_n and σ_s^2 the variance of \mathcal{E}_n
193 with Rician distribution. I_0 is the modified zeroth-order Bessel function of the first kind.³³

194 When larger b-values are used ($b > 1000$ s/mm²), Rician noise is likely to be evident due to the low
195 SNR.³² However, Rician distribution tends toward Gaussian distribution at higher SNRs.^{32,33} Since, as
196 mentioned above, temporal averaging was performed in the present study to improve the SNR of in vivo
197 data and the averaged SNR at the highest b-value ($b = 1000$ s/mm²) was 34.74, that guarantees Gaussian
198 characteristic of the noise. With the Rician model, the marginalized Gaussian likelihood in Eq. (4) is no
199 longer valid. Instead, σ_s^2 should be estimated (estimated from background noise) and S_0 should also
200 be estimated during the subsequent parameter estimation process.

201 2.4. Quantitative Evaluation

202 The effect of Bayesian fitting and low b-values on IVIM parameter mapping was evaluated using
203 several criteria. For simulation results, relative error (RE) for IVIM parameters was calculated at each
204 voxel as follow:

$$205 \text{RE}_{i:n} = \frac{|(G_i - P_i)|}{G_i} \times 100, \quad (8)$$

206 where G_i is the ground-truth, P_i is the predicted IVIM parameters, and i represents the i^{th} pixel.

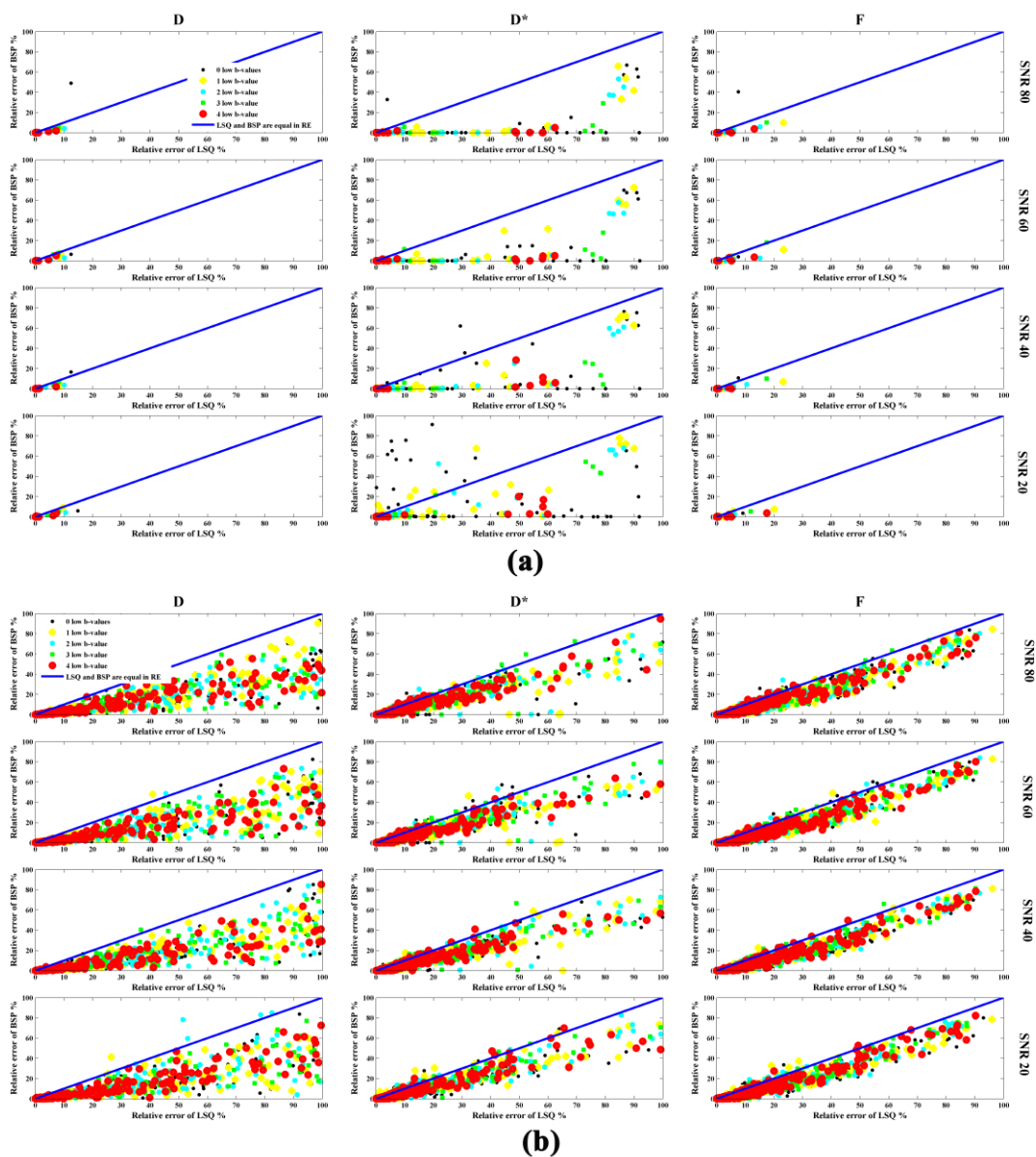
207 The mean values of the parameters estimated with different number of low b-values in the tumor
208 ROI were compared in both simulations and in vivo experiments. Bland-Altman analysis was performed
209 to evaluate the intra-subject reproducibility of two consecutive brain scans. The differences in IVIM
210 parameters between brain tumor and normal ROIs were compared. Finally, statistical significance of
211 differences in parameters between brain tumor and normal ROIs and RE between the fitting methods
212 was tested using two-sample t-test and the fitting methods were implemented in Matlab.

213 The average fitting time for LSQ and BSP is 3×10^{-2} s/ voxel and 4×10^{-1} s/voxel, respectively.
214 All the calculations were performed on a laptop (Inter(R) Core(TM) i7-5500U CPU, 2.40GHz).

215 3. Results

216 3.1. Simulated images

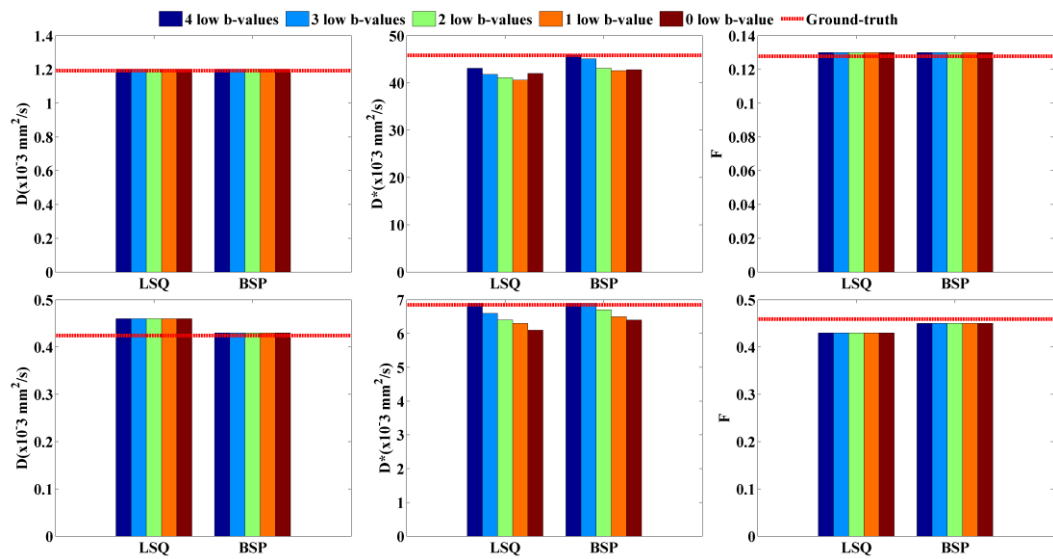
217 Two simulations with different pseudo-diffusion coefficients and Gaussian noise were performed
 218 with different b-value configurations. To show visually the difference between estimated parameters and
 219 ground-truth, in Fig. 2 are given the RE maps. Obviously, in the high-perfusion region (Fig. 2(a)), the
 220 REs generated by BSP are lower than those produced by LSQ for the three IVIM parameters ($p < 0.001$).
 221 When reducing the number of low b-values, the RE of D^* increases, especially with the use of LSQ.
 222 However, the estimation of D or F is insensitive to the number of low b-values. The REs in low-perfusion
 223 regions are shown in Fig. 2(b). Similarly to Fig. 2(a), BSP results in lower error than LSQ, but the
 224 influence of low b-values on D^* estimation was reduced.



225

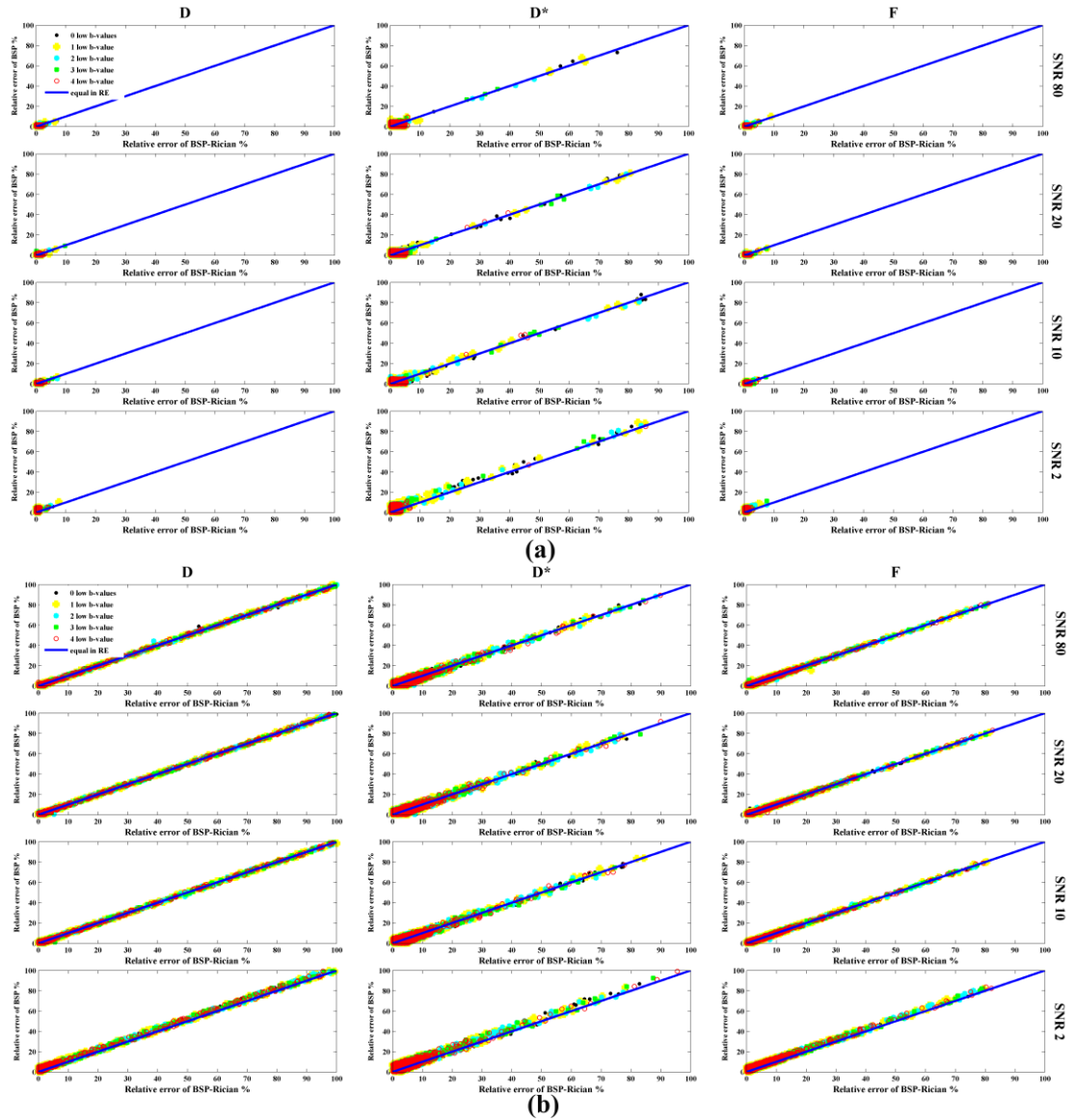
226 Fig. 2. Relative errors (REs) of the estimated IVIM parameters on simulation data with Gaussian noise. (a) REs
 227 in high-perfusion region (b) REs in low-perfusion region. The coordinates of each point represent the RE of each
 228 voxel obtained using the two fitting methods.

229 To further analyze the influence of low b-values on the estimation of IVIM parameters, we
 230 summarize in Fig. 3 the mean values of each parameter obtained by both BSP and LSQ under different
 231 low b-values configurations. As observed, in both high-perfusion region (1st row) and low-perfusion
 232 region (2nd row), the mean of D^* decreases when reducing the number of low b-values, especially in
 233 high-perfusion region. The estimated D^* by BSP is closer to the ground-truth, compared to that by LSQ.
 234 The estimation of D or F was not affected by low b-values.



235
 236 Fig. 3 Mean of IVIM parameters on simulation data with Gaussian noise. The first row represents the
 237 estimated results in high-perfusion regions, and the second row the results in low-perfusion regions.

238 To assess the impact of noise model on IVIM parameter estimation when using BSP method, two
 239 variants of BSP method with two noise models, namely BSP (Gaussian noise model) and BSP-Rician
 240 (Rician noise model) were compared. The results are given in Fig. 4. In both high perfusion region (Fig.
 241 4(a)) and low perfusion region (Fig. 4(b)). Similar results are observed for the two BSP methods with
 242 the two noise models. Although at the low SNR (SNR=2), the RE generated by BSP-Ricain is slightly
 243 smaller than that produced by BSP, the results remain very close.



244

245

Fig. 4. Relative errors (REs) of the estimated IVIM parameters on simulation data with Rician noise. (a) REs in high-perfusion region. (b) REs in low-perfusion region. The coordinates of each point represent the REs of each voxel obtained using the two fitting methods, BSP and BSP-Rician, respectively.

247

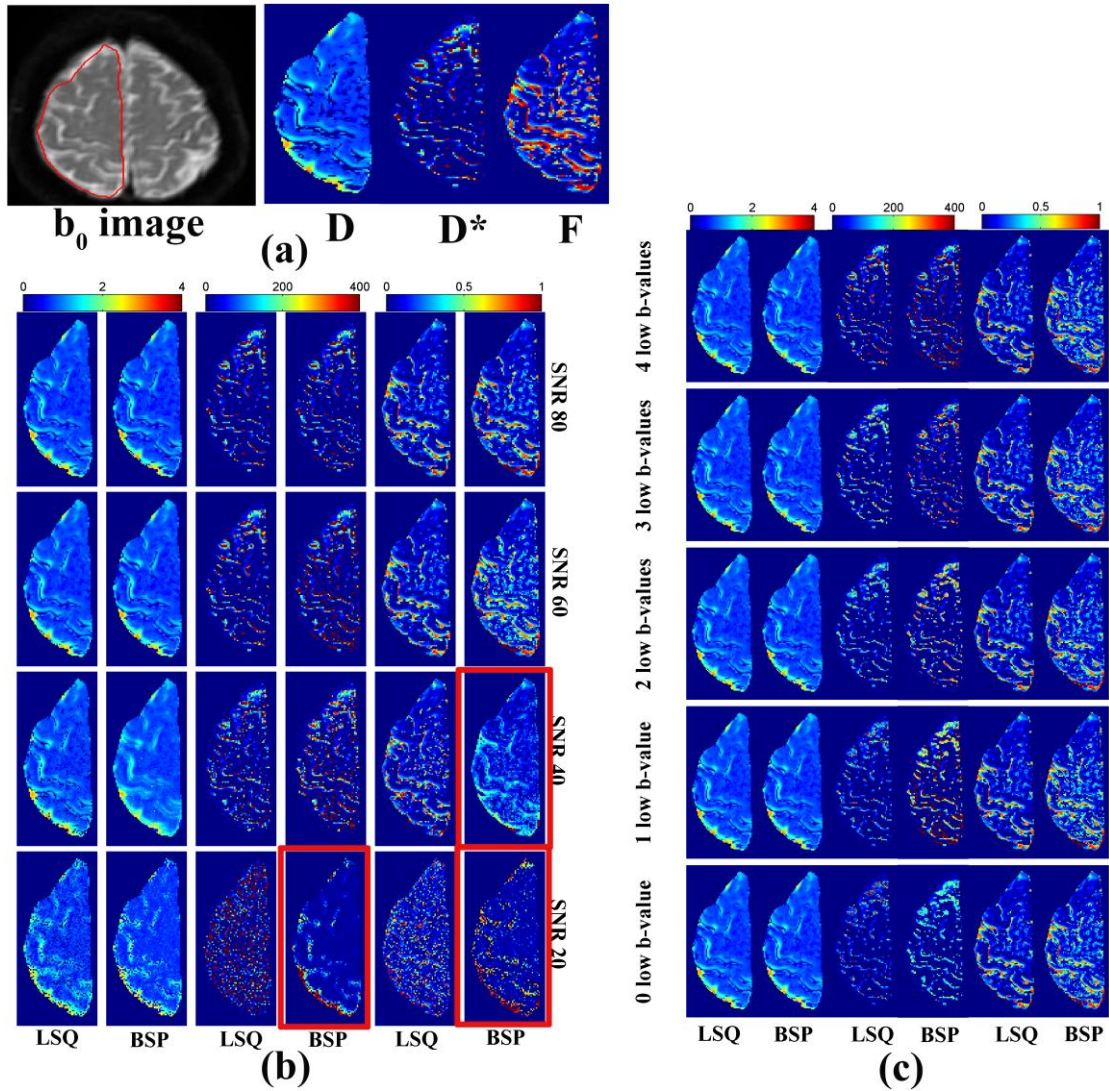
248

The fitting results using different SNRs or different number of low b-values in heterogeneous regions are compared in Figs. 5. In Fig. 5(b), all the parameter maps were obtained using 4 low b-values. When the SNR was decreased, the parameter maps generated by the two fitting methods were heavily corrupted by noise, especially in perfusion-related BSP parameter maps. BSP however generated smoother D^* and F maps than LSQ (red-boxed parameter maps), but induced at the same time information missing. When SNR is higher, the dependence on low b-values of BSP was also lower than that of LSQ in the heterogeneous region, as can be seen in Fig. 5(c). Indeed, when there is no low b-value, D^* maps estimated from LSQ or BSP are far away from ground truth (in particular loss of

254

255

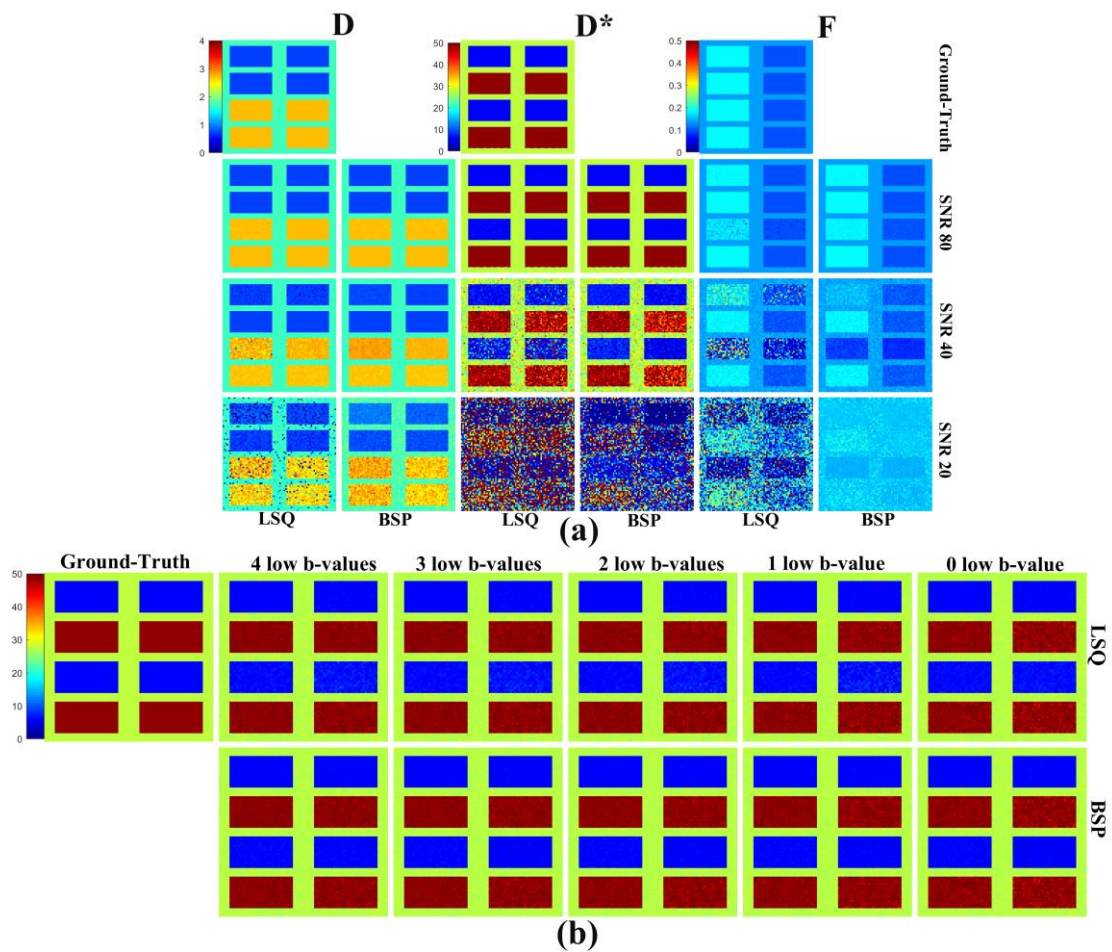
256 higher D^* values). When passing from 4 low b-values to 1 low b-value, D^* map estimated from LSQ
 257 becomes sparser and loses higher D^* values while for BSP, the D^* maps change little and are slightly
 258 smoothed. In all cases, D map and F map vary little with the number of low b-values.
 259



260
 261 Fig. 5. Parameter maps of simulation data in heterogeneous region. (a) B_0 image marked with ROI of a
 262 healthy brain and the corresponding ground-truth parameter maps. (b) Parameter maps generated by LSQ and BSP
 263 using 4 low b-values. (c) An example of parameter maps at SNR 60 and with different number of low b-values.
 264 For (b) and (c), the first two columns represent D , the middle two columns D^* and the last two columns F . The
 265 red-boxed parameter maps show the situation where details are greatly smoothed out when using BSP.

266 The fitting results in homogeneous regions are shown in Fig. 6. Similar results to those in
 267 heterogeneous region were found. BSP generated cleaner parameter maps than LSQ. With the
 268 decreasing of SNR, D^* and F maps of both methods become more and more noisy, the rectangles tend

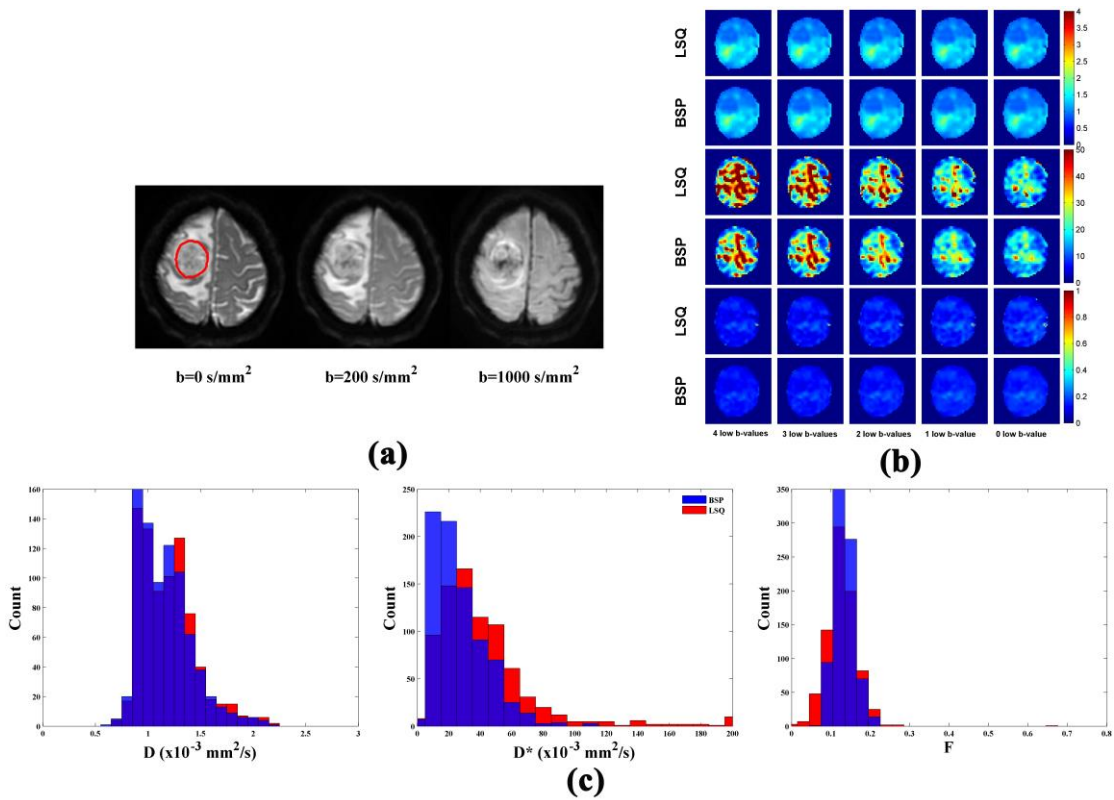
269 to disappear, and the values of some rectangles are altered (Fig. 6(a)). In contrast, D maps change
 270 relatively little although they also become somewhat noisier with the decreasing of SNR. The
 271 comparison of the effect of the number of low b-values on D^* estimation was shown in Fig. 6(b). For
 272 both LSQ and BSP, the estimated D^* in the subregion with high pseudo-diffusion coefficient (red
 273 rectangles) moves away from the ground-truth as the number of low b-values decreased, which is not
 274 the case for the blue and green areas (having relatively low pseudo-diffusion coefficient) that change
 275 little. Nevertheless, although noisier, the shape of the areas remains unchanged.
 276



277
 278 Fig. 6. Parameter maps of simulation data in homogenous regions. (a) Parameter maps generated by LSQ and
 279 BSP using 4 low b-values. (b) D^* maps at SNR 60 and with different number of low b-values. On the top row are
 280 given three ground-truth parameter maps, each of them contains 8 rectangles. In each parameter map of (a) and (b),
 281 different colors represent different homogenous areas. For example, in D^* map, the red rectangles represent the
 282 region with high D^* , the blue rectangles the region with low D^* , and the green areas the region with D^* whose
 283 value is the average of high and low parameter values.

284 **3.2. In vivo images**

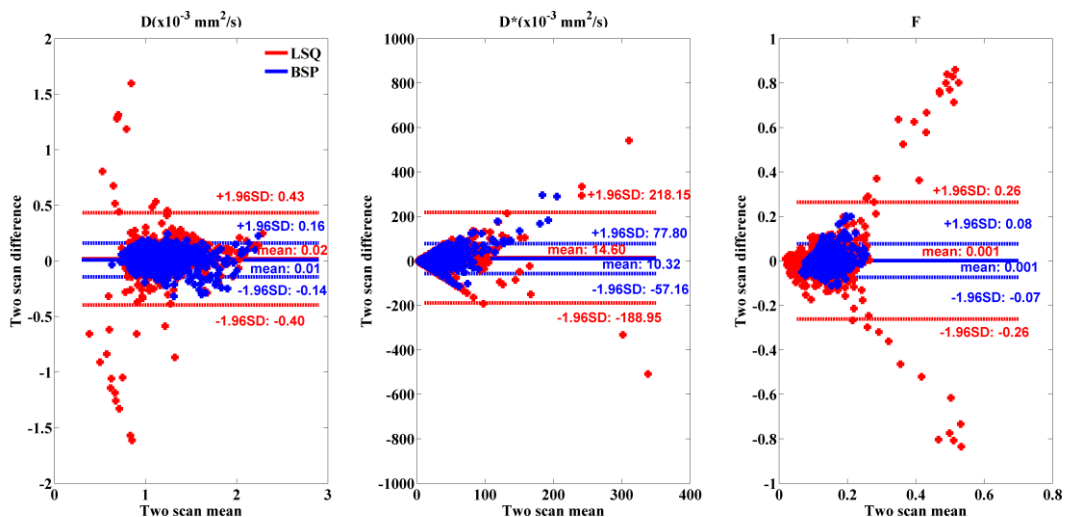
285 The brain DW images marked with the tumor ROI of a meningioma are given in Fig. 7(a). The
 286 IVIM parameter maps of tumor ROI are shown in Fig. 7(b). BSP generates clearer parameter maps
 287 than LSQ. Results similar to simulation results are observed with respect to the effect of low b-values
 288 on parameter estimation. The estimation of D or F map of tumor region is insensitive to low b-values in
 289 comparison with D^* map of tumor region. The estimated D^* decreases with the reduction of the
 290 number of low b-values. The histograms of the obtained parameters are given in Fig. 7(c). The
 291 parameter distributions in the tumor region generated by BSP are more uniform than those by LSQ,
 292 which is reflected by the narrower IVIM parameter distribution of BSP with respect to LSQ. More
 293 outliers at the boundary of the constraints were generated by LSQ.



294
 295 Fig. 7. (a) DW image marked with tumor ROI. (b) IVIM parameter maps of tumor ROI. The first two lines of
 296 (b) represent the parameter D , the middle two rows D^* , and the last two rows F . (c) histograms of parameters in (b)
 297 in the case of using 4 low b-values.

298 Bland-Altman analysis was performed to evaluate the intra-subject reproducibility of consecutive
 299 brain scans. The results on the tumor ROI in Fig. 7 are plotted in Fig. 8, where the mean biases (mean
 300 difference in the estimated parameter between two scans) are as follows. Mean bias in D : (LSQ,

301 BSP)=($+0.02 \times 10^{-3} \text{ mm}^2/\text{s}$, $+0.01 \times 10^{-3} \text{ mm}^2/\text{s}$). Mean bias in F : (LSQ, BSP)=($+0.001$, $+0.001$). Mean
 302 bias in D^* : (LSQ, BSP)=($+14.60 \times 10^{-3} \text{ mm}^2/\text{s}$, $10.32 \times 10^{-3} \text{ mm}^2/\text{s}$). The Bland-Altman repeatability
 303 coefficients (calculated as the half-length of the interval of the 95% confidence interval or limits of
 304 agreement) are the following. Repeatability coefficients for D : (LSQ, BSP)=($0.42 \times 10^{-3} \text{ mm}^2/\text{s}$, 0.15
 305 $\times 10^{-3} \text{ mm}^2/\text{s}$). Repeatability coefficients for F : (LSQ, BSP)=(0.26 , 0.08). Repeatability coefficients for
 306 D^* : (LSQ, BSP)=($203.55 \times 10^{-3} \text{ mm}^2/\text{s}$, $67.48 \times 10^{-3} \text{ mm}^2/\text{s}$). Table 1 summarizes the details of the
 307 Bland-Altman analysis results over all the tumor ROIs. The mean values of bias over four brain tumor
 308 ROIs are the following. Mean bias in D : (LSQ, BSP)=($0.05 \times 10^{-3} \text{ mm}^2/\text{s}$, $0.03 \times 10^{-3} \text{ mm}^2/\text{s}$). Mean
 309 bias in F : (LSQ, BSP)=(0.03 , 0.03). Mean bias in D^* : (LSQ, BSP)=($10.88 \times 10^{-3} \text{ mm}^2/\text{s}$, 3.26×10^{-3}
 310 mm^2/s). The mean values of Bland-Altman repeatability coefficients are as follows. Mean repeatability
 311 coefficients for D : (LSQ, BSP)=($0.92 \times 10^{-3} \text{ mm}^2/\text{s}$, $0.36 \times 10^{-3} \text{ mm}^2/\text{s}$). Mean repeatability
 312 coefficients for F : (LSQ, BSP)=(0.59 , 0.24). Mean repeatability coefficients for D^* : (LSQ,
 313 BSP)=($365.56 \times 10^{-3} \text{ mm}^2/\text{s}$, $27.18 \times 10^{-3} \text{ mm}^2/\text{s}$). BSP exhibits better reproducibility with lower mean
 314 bias, narrower interval of limits of agreement and smaller mean Bland-Altman repeatability coefficient,
 315 compared to LSQ for all three IVIM parameters.



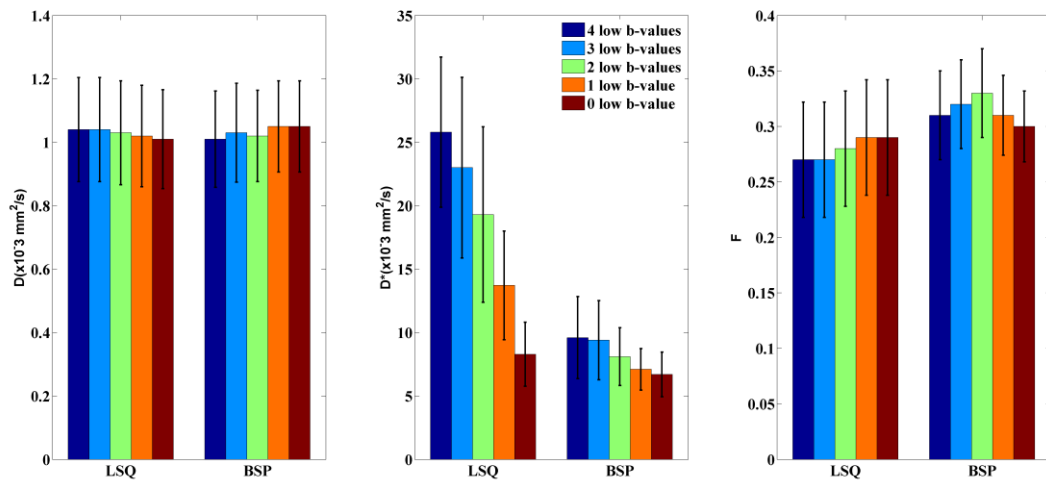
316
 317 Fig. 8. Bland-Altman analysis for the tumor in Fig. 7. The plots show intra-subject reproducibility in the brain
 318 tumor region of two consecutive scans for both LSQ and BSP. The solid lines (red or blue) represent the mean
 319 difference in the estimated parameter between two scans, and the two paired dash (red or blue) lines represent the
 320 limits of agreement (95% confidence interval). Note that the blue BSP points are more tightly clustered, thus
 321 showing higher reproducibility and fewer outliers.

322 **Table 1 Bland-Altman results with bias and limits of agreement (95% confidence interval) for in**
 323 **vivo brain tumor ROIs.**

Subject	$D (\times 10^{-3} \text{ mm}^2/\text{s})$		$D^* (\times 10^{-3} \text{ mm}^2/\text{s})$		F	
	LSQ	BSP	LSQ	BSP	LSQ	BSP
Mean bias						
1	0.02	0.01	14.60	10.32	0.001	0.001
2	-0.08	-0.06	-18	0.33	0.069	0.093
3	0.03	0.03	5.80	0.62	-0.01	-0.02
4	-0.08	-0.02	-5.11	1.78	0.04	-0.03
Mean ^a	0.05	0.03	10.88	3.26	0.03	0.03
P value ^c	0.24	0.30	0.23	0.58	0.45	0.48
Limits of agreement						
1	0.43	0.16	218.15	77.80	0.26	0.08
	-0.40	-0.14	-188.95	-57.16	-0.26	-0.07
2	0.94	0.15	515.89	10.14	0.76	0.31
	-1.10	-0.27	-551.88	-9.48	-0.63	-0.13
3	0.97	0.30	297.86	2.70	0.73	0.24
	-0.91	-0.23	-286.24	-1.47	-0.75	-0.30
4	1.22	0.89	427.65	31.11	0.72	0.35
	-1.39	-0.94	-437.87	-27.55	-0.64	-0.42
Mean ^b	0.92	0.36	365.56	27.18	0.59	0.24

324 **“a”**: Mean value of bias across the four brain tumor ROIs. **“b”**: Mean value of
 325 **Bland-Altman repeatability coefficients across the four brain tumor ROIs. The Bland-Altman**
 326 **repeatability coefficient was calculated as the half-length of the interval of the limits of**
 327 **agreement. “c”**: P values calculated by t-test to assess the significant difference of bias from zero.

328 To further quantitatively analyze the effect of low b-values on parameter estimation, Fig. 9 plots
 329 the means and standard deviations of the parameters obtained over all the brain tumor ROIs. We
 330 observe similar results to the simulations. The estimation of D^* was affected by the number of low
 331 b-values and especially for LSQ method. In contrast, the estimation of D or F was insensitive to low
 332 b-values.



333

334 Fig. 9. The means and standard deviations of IVIM parameters of in vivo brains across all the tumor ROIs.

335 The error bar indicates the standard deviation.

336 The differences in IVIM parameters between tumor and normal brain regions are given in Fig. 10

337 and Fig. 11. The comparison of parameter maps between the tumor in Fig. 7 and its corresponding

338 normal region is shown in Fig. 10. All the parameter maps of the tumor region are clearly different

339 from those of the normal region. It is visually easier to distinguish tumor from normal region in the

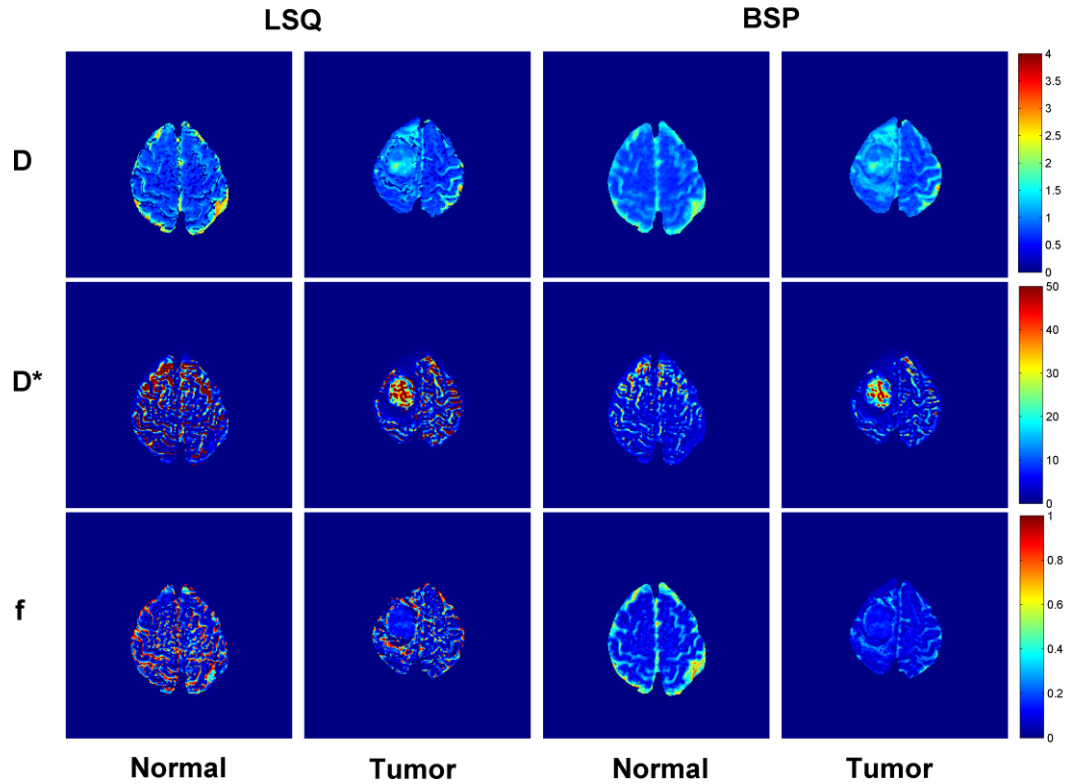
340 results of BSP than in the results of LSQ, due to fewer outliers in the former. More details of IVIM

341 parameter comparison between tumor and normal regions over all the subjects are summarized in Fig.

342 11. Obvious differences are observed between tumor and normal regions in parameters D ($p < 0.05$) and

343 F (especially F , $p < 0.001$). BSP generated fewer outliers with respect to LSQ and distinguished better

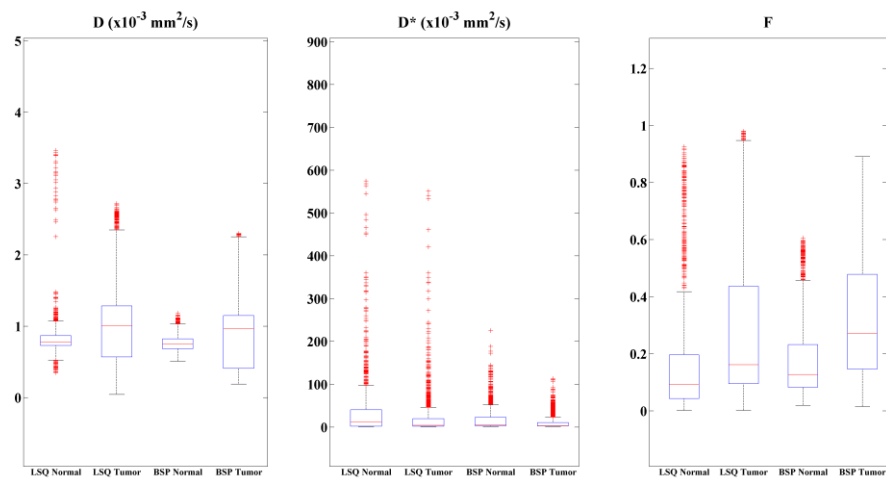
344 tumor from normal regions in parameter F .



345

346

Fig. 10. Comparison of IVM parameter maps between the tumor in Fig. 7 and the corresponding normal region.



347

348

Fig. 11. Box-and-whisker plots summarizing results for all the tumor and normal ROIs.

349 4. Discussion

350 We have investigated IVIM parameter mapping of brain tumors using different low b-value
 351 configurations and fitting methods. It is generally recognized that perfusion information is very
 352 important in the application of IVIM to brain tumors. For example, the higher the tumor stage, the

353 higher the perfusion fraction. Poor accuracy of perfusion-related parameter estimation in previous
354 studies is likely due to the deficiency of nonlinear least squares in solving the regression problem. LSQ
355 aims by essence to obtain IVIM parameters by minimizing the residual between model and fitted
356 signals. The more accurate the estimated parameter, the smaller the residual should be, but not vice
357 versa. This is because different parameters of IVIM model play different role in signal attenuation.
358 Pseudo-diffusion coefficient D^* is much greater than diffusion coefficient D . As a result, the
359 contribution of perfusion component to the signal is weaker than that of diffusion component, due to
360 the exponential IVIM model. That explains why in practice estimating accurately the weak contribution
361 of D^* is difficult and any estimation bias of D^* will inevitably affect the estimation of the other
362 perfusion-related parameter F . The RE map in simulations shows the superiority of Bayesian method:
363 all the parameters obtained by BSP are closer to the ground-truth than those by LSQ, especially for the
364 perfusion-related parameters. This is because BSP solves the regression problem in terms of probability,
365 namely, it outputs the parameter by calculating the maximum posterior probability of signals instead of
366 minimizing signal residual, thus the effect of the weak contribution of D^* to signals on parameter
367 estimation is reduced.

368 To get more stable fitting results, the constraint on the range of parameter values was imposed in
369 LSQ. We however observed an increase of the number of pixels undergoing outlying estimations at the
370 boundary of the constraint. Since the uncertainty of LSQ parameter estimation is determined by the
371 curvature of cost function of the minimization problem, this approach becomes inappropriate if the
372 estimate is on a constraining boundary¹⁹. In contrast, BSP is strong enough to shrink outliers to the
373 means of ROI, as shown in the in vivo experiment. Consequently, the histogram of IVIM parameters
374 obtained by BSP is narrower than that obtained by LSQ due to the reduction of outlying estimations.
375 That explains why BSP generated more uniform parameter maps compared to LSQ. Since BSP
376 generated fewer outliers in parameter estimation, it differentiated better between brain tumor and
377 normal regions.

378 However, whatever it was a heterogeneous region or a homogeneous region, when SNR was
379 relatively low, BSP decreased and such decreasing was reflected by the disappearance of geometrical
380 structures and appearance of quasi-homogeneous areas, though BSP generated fewer outliers with
381 respect to LSQ. The latter however preserved better original heterogeneous parameter characteristics
382 for high SNR and generated random noise-like parameter maps when SNR was low. This is

383 particularly obvious in D^* and F parameter maps for lower SNRs. That can be explained as follows.
384 When SNR decreased, the choice of prior on parameter estimation was critical.²¹ If the prior is far from
385 the ground-truth of IVIM parameter distribution, the estimation of IVIM parameters will become
386 inaccurate, which will be reflected for instance by the disappearance of information in the estimated
387 parameter maps.

388 The obtained results showed that, besides fitting methods, low b-values also played a very
389 important role in the parameter mapping of brain tumors. When low b-values were not used in IVIM
390 parameter estimation, the pseudo-diffusion coefficient D^* of tumor tended to be underestimated. Similar
391 finding was reported by Cohen et al. also in human livers. The difference is that liver is an organ that has
392 relatively high pseudo-diffusion coefficients, and that, as a result, when low b-value acquisitions are
393 absent, the contribution of perfusion component to the signal is near to zero. In this case, different values
394 of D^* may generate close signal residuals, thus yielding underestimated D^* . However,
395 previously-reported studies only considered the LSQ method and the impact of low b-values on D^*
396 estimation in low-perfusion tissue was not addressed. The results in the present work clearly showed that
397 the estimation of D^* by LSQ or BSP was dependent on low b-values, even in the low-perfusion region.
398 Moreover, when using BSP, four low b-values were necessary for high-perfusion regions and three low
399 b-values were in contrast enough for low-perfusion regions. When using LSQ, at least four low b-values
400 were necessary for low-perfusion regions; in other cases, such as high-perfusion regions, even with four
401 low b-values, D^* was underestimated. Hence, LSQ is more susceptible to low b-value than BSP, which
402 was also verified in in vivo experiments.

403 Although BSP presents better performance than LSQ for parameter estimation, it requires more
404 CPU execution time. This may become non-negligible if the amount of data is large.

405 Note that, with respect to the previous investigation about the effect of low b-values on parameter
406 estimation,³⁴ which was focused on the human thigh having relatively higher pseudo-diffusion
407 coefficients, the present work emphasized the accurate IVIM parameter estimation using Bayesian fitting
408 and reduced number of low b-values for the human brain, which is considered as the low-perfusion tissue.
409 The results showed that the number of low b-values is also very important for IVIM applications on
410 low-perfusion tissue, and that Bayesian fitting allows clearly differentiating brain tumors from normal
411 regions. Moreover, BSP requires less low b-values than LSQ, which also means shorter acquisition time.

412 Finally, the assumption on noise model should be taken into account in the use of the BSP method.
413 In the present study, similar results were obtained when using BSP (Gaussian noise model) and
414 BSP-Rician (Rician noise model) at higher SNRs. This is likely because Rician distribution tends
415 toward Gaussian distribution at higher SNRs.^{32, 33} When SNR is low, Rician distribution is closer to the
416 actual noise model and the BSP-Rician model was more suitable for parameter estimation.

417 **5. Conclusions**

418 IVIM parameters allow clearly brain tumors to be differentiated from normal regions. Bayesian
419 fitting yields robust IVIM parameter mapping with fewer outliers. Both BSP and LSQ fittings require
420 enough number of low b-values for the accurate estimation of perfusion parameters of brain tumors, but
421 BSP requires less low b-values than LSQ, which also represents shorter acquisition time.

422 **Acknowledgements**

423 This work was funded in part by the National Nature Science Foundations of China (Grant No.
424 61762019, 61661010, 81701654), the Funds for Talents of Guizhou University (No. 2013-33), the
425 Nature Science Foundation of Guizhou province (Qiankehe J No.20152044, [2016]1096), and the
426 Program PHC-Cai Yuanpei 2018 (N° 41400TC).

427 **Conflict of Interest Statement**

428 None declared.

429 **References**

- 430 ¹ D. Le Bihan, E. Breton, D. Lallemand, P. Grenier, E. Cabanis, and M. Laval_Jeantet, MR
431 imaging of Intravoxel Incoherent Motions: Application to Diffusion and Perfusion in Neurologic
432 Disorders, *Radiology* **161**(2), 401–407 (1986).
- 433 ² S. Bisdas, T.S. Koh, C. Roder, *et al.*, Intravoxel incoherent motion diffusion-weighted MR
434 imaging of gliomas: Feasibility of the method and initial results, *Neuroradiology* **55**(10), 1189–
435 1196 (2013).

436 ³ C. Federau, R. Meuli, K. O'Brien, P. Maeder, and P. Hagmann, Perfusion measurement in brain
437 gliomas with intravoxel incoherent motion MRI, *Am. J. Neuroradiol.* **35**(2), 256–262 (2014).

438 ⁴ C. Federau, K. O'Brien, R. Meuli, P. Hagmann, and P. Maeder, Measuring brain perfusion with
439 intravoxel incoherent motion (IVIM): Initial clinical experience, *J. Magn. Reson. Imaging* **39**(3),
440 624–632 (2014).

441 ⁵ A. Catanese, F. Malacario, L. Cirillo, *et al.*, Application of intravoxel incoherent motion (IVIM)
442 magnetic resonance imaging in the evaluation of primitive brain tumours, *Neuroradiol. J.* **31**(1),
443 4–9 (2018).

444 ⁶ H.S. Kim, C.H. Suh, N. Kim, C.G. Choi, and S.J. Kim, Histogram analysis of intravoxel
445 incoherent motion for differentiating recurrent tumor from treatment effect in patients with
446 glioblastoma: Initial clinical experience, *Am. J. Neuroradiol.* **35**(3), 490–497 (2014).

447 ⁷ E.M. Meeus, J. Novak, S.B. Withey, N. Zarinabad, H. Dehghani, and A.C. Peet, Evaluation of
448 intravoxel incoherent motion fitting methods in low-perfused tissue, *J. Magn. Reson. Imaging*
449 **45**(5), 1325–1334 (2017).

450 ⁸ A. Andreou, D.M. Koh, D.J. Collins, *et al.*, Measurement reproducibility of perfusion fraction
451 and pseudodiffusion coefficient derived by intravoxel incoherent motion diffusion-weighted MR
452 imaging in normal liver and metastases, *Eur. Radiol.* **23**(2), 428–434 (2013).

453 ⁹ Z.X. Kuai, W.Y. Liu, Y.L. Zhang, and Y.M. Zhu, Generalization of intravoxel incoherent motion
454 model by introducing the notion of continuous pseudodiffusion variable, *Magn. Reson. Med.*
455 **76**(5), 1594–1603 (2016).

456 ¹⁰ C. Federau, P. Maeder, K. O'Brien, P. Browaeys, R. Meuli, and P. Hagmann, Quantitative
457 Measurement of Brain Perfusion with Intravoxel Incoherent Motion MR Imaging, *Radiology*
458 **265**(3), 874–881 (2012).

459 ¹¹ C. Federau and K. O'Brien, Increased brain perfusion contrast with T2-prepared intravoxel
460 incoherent motion (T2prep IVIM) MRI, *NMR Biomed.* **28**(1), 9–16 (2015).

461 ¹² V.C. Keil, B. Mädler, G.H. Gielen, *et al.*, Intravoxel incoherent motion MRI in the brain: Impact
462 of the fitting model on perfusion fraction and lesion differentiability, *J. Magn. Reson. Imaging*
463 **46**(4), 1187–1199 (2017).

464 ¹³ P.T. While, A comparative simulation study of bayesian fitting approaches to intravoxel
465 incoherent motion modeling in diffusion-weighted MRI, *Magn. Reson. Med.* **00**, 1–15 (2017).

466 ¹⁴ G.Y. Cho, L. Moy, J.L. Zhang, *et al.*, Comparison of fitting methods and b-value sampling
467 strategies for intravoxel incoherent motion in breast cancer, *Magn. Reson. Med.* **74**(4), 1077–
468 1085 (2015).

469 ¹⁵ H. Merisaari, P. Movahedi, I.M. Perez, *et al.*, Fitting methods for intravoxel incoherent motion
470 imaging of prostate cancer on region of interest level: Repeatability and gleason score prediction,
471 *Magn. Reson. Med.* **77**(3), 1249–1264 (2017).

472 ¹⁶ R. Fusco, M. Sansone, and A. Petrillo, A comparison of fitting algorithms for diffusion-weighted
473 MRI data analysis using an intravoxel incoherent motion model, *Magn. Reson. Mater. Physics,*
474 *Biol. Med.* **30**(2), 113–120 (2017).

475 ¹⁷ H.J. Park, Y.S. Sung, S.S. Lee, *et al.*, Intravoxel incoherent motion diffusion-weighted MRI of
476 the abdomen: The effect of fitting algorithms on the accuracy and reliability of the parameters, *J.*
477 *Magn. Reson. Imaging* **45**(6), 1637–1647 (2017).

478 ¹⁸ M. Freiman, J.M. Perez-Rossello, M.J. Callahan, *et al.*, Reliable estimation of incoherent motion
479 parametric maps from diffusion-weighted MRI using fusion bootstrap moves, *Med. Image Anal.*
480 **17**(3), 325–336 (2013).

481 ¹⁹ M.R. Orton, D.J. Collins, D.-M. Koh, and M.O. Leach, Improved intravoxel incoherent motion
482 analysis of diffusion weighted imaging by data driven Bayesian modeling., *Magn. Reson. Med.*
483 **71**(1), 411–20 (2014).

484 ²⁰ G.R. Spinner, C. Von Deuster, K.C. Tezcan, C.T. Stoeck, and S. Kozerke, Bayesian intravoxel
485 incoherent motion parameter mapping in the human heart, *J. Cardiovasc. Magn. Reson.* **19**(1), 1–
486 14 (2017).

487 ²¹ O. Gustafsson, M. Montelius, G. Starck, and M. Ljungberg, Impact of prior distributions and
488 central tendency measures on Bayesian intravoxel incoherent motion model fitting, *Magn.*
489 *Reson. Med.* **00**, 1–10 (2017).

490 ²² A.D. Cohen, M.C. Schieke, M.D. Hohenwarter, and K.M. Schmainda, The effect of low b-values
491 on the intravoxel incoherent motion derived pseudodiffusion parameter in liver, *Magn. Reson.*
492 *Med.* **73**(1), 306–311 (2015).

493 ²³ G. Gambarota, E. Hitti, B. Leporq, H. Saint-Jalmes, and O. Beuf, Eliminating the blood-flow
494 confounding effect in intravoxel incoherent motion (IVIM) using the non-negative least square
495 analysis in liver, *Magn. Reson. Med.* **77**(1), 310–317 (2017).

496 ²⁴ A.M. Chow, D.S. Gao, S.J. Fan, *et al.*, Liver fibrosis: An intravoxel incoherent motion (IVIM)
497 study, *J. Magn. Reson. Imaging* **36**(1), 159–167 (2012).

498 ²⁵ S. Colagrande, F. Pasquinelli, L.N. Mazzoni, G. Belli, and G. Virgili, MR-diffusion weighted
499 imaging of healthy liver parenchyma: Repeatability and reproducibility of apparent diffusion
500 coefficient measurement, *J. Magn. Reson. Imaging* **31**(4), 912–920 (2010).

501 ²⁶ R. van der Bel, O.J. Gurney-Champion, M. Froeling, E.S.G. Stroes, A.J. Nederveen, and C.T.P.
502 Krediet, A tri-exponential model for intravoxel incoherent motion analysis of the human kidney:
503 In silico and during pharmacological renal perfusion modulation, *Eur. J. Radiol.* **91**(March),
504 168–174 (2017).

505 ²⁷ T. Finkenstaedt, M. Klarhoefer, C. Eberhardt, *et al.*, The IVIM signal in the healthy cerebral gray
506 matter: A play of spherical and non-spherical components, *Neuroimage* **152**, 340–347 (2017).

507 ²⁸ S. Bisdas and U. Klose, IVIM analysis of brain tumors: an investigation of the relaxation effects
508 of CSF, blood, and tumor tissue on the estimated perfusion fraction, *Magn. Reson. Mater.*
509 *Physics, Biol. Med.* **28**(4), 377–383 (2015).

510 ²⁹ J. Sijbers, P. Scheunders, N. Bonnet, D. Van Dyck, and E. Raman, Quantification and
511 improvement of the signal-to-noise ratio in a magnetic resonance image acquisition procedure,
512 *Magn. Reson. Imaging* **14**(10), 1157–1163 (1996).

513 ³⁰ M. Bertleff, S. Domsch, S. Weingärtner, *et al.*, Diffusion parameter mapping with the combined
514 intravoxel incoherent motion and kurtosis model using artificial neural networks at 3 T, *NMR*
515 *Biomed.* **30**(12), 1–11 (2017).

516 ³¹ A. Boss, B. Barth, L. Fili, *et al.*, Simultaneous multi-slice echo planar diffusion weighted
517 imaging of the liver and the pancreas: Optimization of signal-to-noise ratio and acquisition time
518 and application to intravoxel incoherent motion analysis, *Eur. J. Radiol.* **85**(11), 1948–1955
519 (2016).

520 ³² S. Walker- Samuel, M. Orton, L.D. McPhail, and S.P. Robinson, Robust estimation of the
521 apparent diffusion coefficient (ADC) in heterogeneous solid tumors, *Magn. Reson. Med. An Off.*
522 *J. Int. Soc. Magn. Reson. Med.* **62**(2), 420–429 (2009).

523 ³³ H. Gudbjartsson and S. Patz, The Rician distribution of noisy MRI data, *Magn. Reson. Med.*
524 **34**(6), 910–914 (1995).

525 ³⁴ C. Ye, D. Xu, Y. Qin, *et al.*, Estimation of intravoxel incoherent motion parameters using low
526 b-values, *PLoS One* **14**(2), 1–16 (2019).

527

528 **Figure Captions**

529 Fig. 2 Flowchart of BSP fitting.

530

531 Fig. 2. Relative errors (REs) of the estimated IVIM parameters on simulation data with Gaussian noise.
532 (a) REs in high-perfusion region (b) REs in low-perfusion region. The coordinates of each point
533 represent the RE of each voxel obtained using the two fitting methods.

534

535 Fig. 3 Mean of IVIM parameters on simulation data with Gaussian noise. The first row represents the
536 estimated results in high-perfusion regions, and the second row the results in low-perfusion regions.

537

538 Fig. 4. Relative errors (REs) of the estimated IVIM parameters on simulation data with Rician noise. (a)
539 REs in high-perfusion region. (b) REs in low-perfusion region. The coordinates of each point represent
540 the REs of each voxel obtained using the two fitting methods, BSP and BSP-Rician, respectively.

541

542 Fig. 5. Parameter maps of simulation data in heterogeneous region. (a) B0 image marked with ROI of a
543 healthy brain and the corresponding ground-truth parameter maps. (b) Parameter maps generated by LSQ
544 and BSP using 4 low b-values. (c) An example of parameter maps at SNR 60 and with different number
545 of low b-values. For (b) and (c), the first two columns represent D , the middle two columns D^* and the
546 last two columns F . The red-boxed parameter maps show the situation where details are greatly smoothed
547 out when using BSP.

548

549 Fig. 6. Parameter maps of simulation data in homogenous regions. (a) Parameter maps generated by LSQ
550 and BSP using 4 low b-values. (b) D^* maps at SNR 60 and with different number of low b-values. On the
551 top row are given three ground-truth parameter maps, each of them contains 8 rectangles. In each
552 parameter map of (a) and (b), different colors represent different homogenous areas. For example, in D^*
553 map, the red rectangles represent the region with high D^* , the blue rectangles the region with low D^* ,
554 and the green areas the region with D^* whose value is the average of high and low parameter values.

555

556 Fig. 7. (a) DW image marked with tumor ROI. (b) IVIM parameter maps of tumor ROI. The first two
557 lines of (b) represent the parameter D , the middle two rows D^* , and the last two rows F . (c) histograms of
558 parameters in (b) in the case of using 4 low b-values.

559

560 Fig. 8. Bland-Altman analysis for the tumor in Fig. 7. The plots show intra-subject reproducibility in the
561 brain tumor region of two consecutive scans for both LSQ and BSP. The solid lines (red or blue)
562 represent the mean difference in the estimated parameter between two scans, and the two paired dash (red
563 or blue) lines represent the limits of agreement (95% confidence interval). Note that the blue BSP points
564 are more tightly clustered, thus showing higher reproducibility and fewer outliers.

565

566 Fig. 9. The means and standard deviations of IVIM parameters of in vivo brains across all the tumor
567 ROIs. The error bar indicates the standard deviation.

568

569 Fig. 10. Comparison of IVM parameter maps between the tumor in Fig. 7 and the corresponding
570 normal region.

571

572 Fig. 11. Box-and-whisker plots summarizing results for all the tumor and normal ROIs.

573